Revision 3

Ab initio study of water speciation in forsterite: importance of the entropic effect

Authors: Tian Qin[1,2], Renata M. Wentzcovitch[2,3], Koichiro Umemoto[4], Marc M. Hirschmann[1], and David L. Kohlstedt[1]

Affiliations:

1. Department of Earth Sciences, University of Minnesota, 116 Church Street SE, Minneapolis, Minnesota 55455, USA.
2. Department of Earth and Environmental Sciences, Columbia University, Lamont-Doherty Earth Observatory, Palisades, NY 10964, USA
3. Department of Applied Physics and Applied Mathematics, Columbia University, New York City, NY 10027, USA
4. Earth-Life Science Institute, Tokyo Institute of Technology, 2-12-1-IE-12 Ookayama, Meguro-ku, Tokyo 152-8550, Japan.

Abstract

In this *ab initio* study, we expand previous investigations of charge-balanced hydrous Mg ($(2\mathrm{H})^{\mathrm{x}}_{\mathrm{Mg}}$) and Si ($(4\mathrm{H})^{\mathrm{x}}_{\mathrm{Si}}$) defects in forsterite, the Mg end-member of olivine, to address the relative stability of these two defects. First, we systematically search for $(2\mathrm{H})^{\mathrm{x}}_{\mathrm{Mg}}$ configurations to find possible defect states; second, we include the contribution of vibrational energy and defect configurational entropy in the calculation of formation energies of both defects; third, we address the effect of pressure and

temperature simultaneously on their relative stability. Based on these considerations, we demonstrate that hydrous Mg defects ($(2\mathrm{H})^{\mathrm{x}}_{\mathrm{Mg}}$) can be stabilized with respect to hydrous Si defects ($(4\mathrm{H})^{\mathrm{x}}_{\mathrm{Si}}$) at relevant mantle conditions and that configurational entropy and vibrational free energy play key roles in this stabilization. Our results reveal that water speciation in olivine is influenced by temperature and pressure. As mantle physical and chemical properties may be affected by the speciation of water in olivine, application of experimental results to the mantle should account for the temperature and pressure dependent changes in water speciation.

Keywords: hydrous defects, olivine, nominally anhydrous minerals, *ab initio* calculations, thermodynamics

Introduction

A unique feature of our planet in the solar system is that over 70% of its surface is covered by liquid water, which is an essential factor of its habitability. Over the decades, it has become evident that water is not only present at Earth's surface, but is also stored in large quantities in its interior (Martin and Donnay 1972; Bell and Rossman 1992; Smyth 1994; Kohlstedt et al. 1996; Bolfan-Casanova 2005). Recently, a ringwoodite inclusion in diamond revealed that the mantle transition zone is at least locally "wet" with near 1 w% H_2O (Pearson et al. 2014). Plate tectonics is responsible for the deep-Earth water cycle, carrying hydrous minerals and water bearing sediments into the mantle via the subduction process. Water then returns to the surface/atmosphere by magmatic degassing beneath mid-ocean ridges and oceanic islands (Peacock 1990; Ohtani 2005). Most of the water in Earth's surface today might come from the degassing of the Earth's mantle through volcanism shortly after the Earth formed (Rubey 1951).

Water is transported into the mantle during subduction chiefly as hydroxyl groups in hydrous silicate minerals (Peacock 1990; Ohtani 2005; van Keken et al. 2011; Nishi et al. 2014). As most hydrous minerals are not stable along the normal mantle geotherm, water delivered to the convecting mantle is believed to be stored chiefly as hydrous defects (hydroxyl point defects) in minerals that do not contain hydrogen in their stoichiometric formulae. These so-called nominally anhydrous minerals (NAMs) include olivine, pyroxene and garnet (Bell and Rossman 1992). Though present in modest concentrations, these defects dramatically influence the physical and chemical properties of their hosts, including the electrical conductivity (Karato 1990; Wang et al. 2006; Yoshino and Katsura 2013) and viscosity (Carter and Ave'lallemant 1970; Chopra and Paterson 1984; Karato et al. 1986; Mei and Kohlstedt 2000a, 2000b), the latter having a strong effect on mantle processes such as convection. Water also decreases the solidus temperature of mantle rocks and, consequently, the extent and composition of partial melting (Kushiro 1972; Green 1973; Hirose 1997).

To understand the influence of water on mantle properties, the mechanisms of water incorporation in olivine, the most voluminous mineral in the upper mantle, must be clarified. In the past few decades, this problem has been addressed by various methods, for example, IR spectroscopy (Bai and Kohlstedt 1992, 1993; Matveev et al. 2001; Lemaire et al. 2004; Berry et al. 2005; Smyth et al. 2006; Kudoh et al. 2006; Hushur et al. 2009; Kovács et al. 2010; Otsuka and Karato 2011; Ingrin et al. 2013; Balan et al. 2014; Tollan et al. 2017; Blanchard et al. 2017), Raman spectroscopy (Bolfan-Casanova et al. 2014), NMR spectroscopy (Kohn 1996; Xue et al. 2017), and theoretical calculations (Wright and Catlow 1994; Brodholt 1997; Haiber et al. 1997; Braithwaite et al. 2002, 2003, Walker et al. 2006, 2007; Umemoto et al. 2011). Several water incorporation mechanisms in olivine have been proposed. Among them, the most likely ones are the formation of hydroxyl groups (OH^-) associated with vacant Mg and Si vacancies (Wright and Catlow 1994; Haiber et al. 1997; Brodholt and Refson 2000; Braithwaite et al. 2003; Walker et al. 2006, 2007; Umemoto et al. 2011; Tollan et al. 2017), represented respectively as $(2\mathrm{H})^{\mathrm{x}}_{\mathrm{Mg}}$ and

$(4\mathrm{H})_{\mathrm{Si}}^{\mathrm{x}}$ with the Kröger-Vink notation (Kröger and Vink 1956). These defects in forsterite, the Mg end member of olivine, have been investigated extensively. Nevertheless, a long-standing debate remains concerning the relative thermodynamic stability of these defects (Hirschmann and Kohlstedt 2012). Measurements of cation diffusion and hydrogen solubility in olivine suggest that hydrous defects are chiefly associated with metal (Mg and Fe) vacancies (octahedral vacancies) (Kohlstedt and Mackwell 1998; Demouchy and Mackwell 2003). In contrast, IR spectroscopy (Matveev et al. 2001; Lemaire et al. 2004; Berry et al. 2005; Kovács et al. 2010; Ingrin et al. 2013; Balan et al. 2014; Tollan et al. 2017) and NMR (Xue et al. 2017) indicate that hydrous defects associated with the Si vacancy dominate in olivine. Also, *ab initio* calculations have consistently indicated that the Si hydrous defect, $(4\mathrm{H})_{\mathrm{Si}}^{\mathrm{x}}$, is energetically favored over the Mg defect, $(2\mathrm{H})_{\mathrm{Mg}}^{\mathrm{x}}$, (Brodholt and Refson 2000; Walker et al. 2007; Umemoto et al. 2011; Balan et al. 2017) .

In this *ab initio* study, we expand previous investigations of the charge-balanced hydrous Mg and Si defects, $(2\mathrm{H})_{\mathrm{Mg}}^{\mathrm{x}}$ and $(4\mathrm{H})_{\mathrm{Si}}^{\mathrm{x}}$, in forsterite ($Mg_2SiO_4$) to address their relative stability. First, we explore systematically the configurations for the $(2\mathrm{H})_{\mathrm{Mg}}^{\mathrm{x}}$ defect. Multiple possible configurations of both $(2\mathrm{H})_{\mathrm{Mg}}^{\mathrm{x}}$ and $(4\mathrm{H})_{\mathrm{Si}}^{\mathrm{x}}$ are considered in this study; second, we include the contribution of vibrational free energy and defect configurational entropy in the calculation of formation energies of these defects; third, we address the effect of pressure and temperature simultaneously on their relative stability. Based on these results, we demonstrate that the Mg defect may be stabilized with respect to Si defect at relevant mantle conditions. We conclude that vibrational free energy, configurational entropy, and proper identification of the configurations of these defects are essential to determining the relative stability field of hydrous defects.

Methods

Chemical reactions to create these hydrous defects

To investigate the relative stability of $(2\mathrm{H})^{\mathrm{x}}_{\mathrm{Mg}}$ and $(4\mathrm{H})^{\mathrm{x}}_{\mathrm{Si}}$ defects, the formation energies are calculated from the following two reactions between forsterite and water:

$$\mathrm{H_2O} + 16\mathrm{Mg_2SiO_4} = \mathrm{H_2Mg_{31}Si_{16}O_{64}} + \mathrm{MgO}\ \#(1)$$

$$2\mathrm{H_2O} + 16\mathrm{Mg_2SiO_4} = \mathrm{H_4Mg_{32}Si_{15}O_{64}} + \mathrm{SiO_2}\#(2).$$

Here, H_2O is an isolated water molecule, and Mg_2SiO_4 is forsterite; the products $\mathrm{H_2Mg_{31}Si_{16}O_{64}}$ and $\mathrm{H_4Mg_{32}Si_{15}O_{64}}$ are hydrogen-bearing olivine with two protons associated with a Mg vacancy and four protons associated with a Si vacancy, respectively. At upper mantle conditions, MgO and SiO_2 in these equations further react with pyroxene ($MgSiO_3$) or forsterite (Mg_2SiO_4), respectively, such that these reactions become

$$\mathrm{H_2O} + \mathrm{MgSiO_3} + 15\mathrm{Mg_2SiO_4} = \mathrm{H_2Mg_{31}Si_{16}O_{64}}\ \#(3)$$

$$2\mathrm{H_2O} + 17\mathrm{Mg_2SiO_4} = \mathrm{H_4Mg_{32}Si_{15}O_{64}} + 2\mathrm{MgSiO_3}\#(4).$$

Therefore, the formation energies of one $(2\mathrm{H})^{\mathrm{x}}_{\mathrm{Mg}}$ ($G_{\mathrm{r}}^{(2\mathrm{H})^{\mathrm{x}}_{\mathrm{Mg}}}$) and one $(4\mathrm{H})^{\mathrm{x}}_{\mathrm{Si}}$ ($G_{\mathrm{r}}^{(4\mathrm{H})^{\mathrm{x}}_{\mathrm{Si}}}$) defect, without considering the lattice configurational entropy are given by

$$G_{\mathrm{r}}^{(2\mathrm{H})^{\mathrm{x}}_{\mathrm{Mg}}} = G_{\mathrm{H_2Mg_{31}Si_{16}O_{64}}} - \left(G_{\mathrm{H_2O}} + G_{\mathrm{MgSiO_3}} + 15G_{\mathrm{Mg_2SiO_4}}\right)\#(5)$$

$$G_{\mathrm{r}}^{(4\mathrm{H})^{\mathrm{x}}_{\mathrm{Si}}} = G_{\mathrm{H_4Mg_{32}Si_{15}O_{64}}} + 2G_{\mathrm{MgSiO_3}} - \left(2G_{\mathrm{H_2O}} + 17G_{\mathrm{Mg_2SiO_4}}\right)\#(6).$$

Since we are interested in the relative stability of these defects, the quantity ΔG_{r} is calculated as $Eq.(6) - 2 \times Eq.(5)$, which results in the same reaction considered by Walker et al (2007) in their Eq. (3). Here, Gibbs free energies of all phases are obtained by *ab initio* computations. The hydrous defects

$H_2Mg_{31}Si_{16}O_{64}$ and $H_4Mg_{32}Si_{15}O_{64}$ are investigated using a 2x1x2 supercell of forsterite with 2 and 4 protons substituting for one Mg or Si cation, respectively. Seven previously identified configurations for the $(4H)_{Si}^{x}$ defect (Brodholt and Refson 2000; Walker et al. 2007; Verma and Karki 2009; Umemoto et al. 2011; Xue et al. 2017) and nine configurations of the $(2H)_{Mg}^{x}$defect are considered in our calculations and illustrated in Fig. 1.

Gibbs free energy

The partition function for the system with multiple configurations of one type of defect can be expressed as (Umemoto et al. 2010)

$$Z_{\mathrm{QHA}}(V,T) = \sum_{i=1}^{N_c} w_i \exp\left(-\frac{E_i(V)}{k_B T}\right) \cdot \prod_{j=1}^{N_{mode}} \left\{ \sum_{v_{i,j}=0}^{\infty} \exp\left[-\left(v_{i,j}+\frac{1}{2}\right)\frac{\hbar\omega_{i,j}(V)}{k_B T}\right]\right\}$$

$$= \sum_{i=1}^{N_c} w_i \exp\left(-\frac{E_i(V)}{k_B T}\right) \cdot \prod_{j=1}^{N_{mode}} \left[\frac{\exp\left(-\frac{\hbar\omega_{i,j}(V)}{2k_B T}\right)}{1-\exp\left(-\frac{\hbar\omega_{i,j}(V)}{k_B T}\right)}\right] \#(7).$$

Here, N_c is the total number of inequivalent configurations, N_{mode} is the number of vibrational modes of a given crystal structure, $E_i(V)$ and w_i are the energy and degeneracy of the i^{th} symmetrically inequivalent configuration, $v_{i,j}$ and $\omega_{i,j}$ are the number of excited phonons and the frequency of j^{th} mode for the i^{th} configuration, $\hbar$ and k_B are the Planck and Boltzmann constants, and *T* is the temperature in Kelvin. As calculating the vibrational density of state (VDOS) of hydrogen-bearing olivine for every symmetrically inequivalent configuration is computational resource demanding, we use a single VDOS for all $(2H)_{Mg}^{x}$ defects and another for all $(4H)_{Si}^{x}$ defects. These VDOSs were obtained using the lowest energy configurations. As shown in Fig. 2, the VDOS for pure olivine and olivine with $(2H)_{Mg}^{x}$ and $(4H)_{Si}^{x}$ are similar, except for peaks associated with OH^- modes. The partition function then changes to (Umemoto et al. 2010; Shukla and Wentzcovitch 2016)

$$Z_{\mathrm{QHA}}(V,T) = \left[\sum_{\mathrm{i}=1}^{\mathrm{N_c}} \mathrm{w_i} \exp\left(-\frac{E_{\mathrm{i}}(V)}{k_{\mathrm{B}}T}\right)\right] \cdot \left\{\prod_{\mathrm{j}=1}^{\mathrm{N_{mode}}} \left[\frac{\exp\left(-\frac{\hbar\omega_{\mathrm{j}}(V)}{2k_{\mathrm{B}}T}\right)}{1-\exp\left(-\frac{\hbar\omega_{\mathrm{j}}(V)}{k_{\mathrm{B}}T}\right)}\right]\right\} \#(8).$$

This approximate partition function can be used to obtain the Helmholtz free energy $F(V,T) = -k_{\mathrm{B}}T\ln\left[Z_{\mathrm{QHA}}(V,T)\right]$, the pressure $P(V,T) = -\left(\frac{\partial F(V,T)}{\partial \mathrm{V}}\right)_{\mathrm{T}}$, and then the Gibbs free energy $G(P,T) = F(V,T) + P(V,T)V$, including the internal configurational entropy, but exclusive of the lattice configurational entropy.

Lattice configurational entropy

A key ingredient in this study is the (lattice) configurational entropy. Since one $(4\mathrm{H})^{\mathrm{x}}_{\mathrm{Si}}$ contains four protons and one $(2\mathrm{H})^{\mathrm{x}}_{\mathrm{Mg}}$ contains two, twice the number of $(2\mathrm{H})^{\mathrm{x}}_{\mathrm{Mg}}$ defects as $(4\mathrm{H})^{\mathrm{x}}_{\mathrm{Si}}$ defects are required to account for a given amount of hydrogen. Therefore, the lattice configurational ("mixing") entropies are different, which changes the relative formation energies of $(2\mathrm{H})^{\mathrm{x}}_{\mathrm{Mg}}$ and $(4\mathrm{H})^{\mathrm{x}}_{\mathrm{Si}}$ defects as well as their relative stabilities. At low defect concentrations, defect-defect interactions are expected to be negligible and the configurational entropy is

$$S^{\mathrm{v}}_{\mathrm{conf}} = -R[(1-\mathrm{x_v})\ln(1-\mathrm{x_v}) + \mathrm{x_v}\ln\mathrm{x_v}] \#(9),$$

where $\mathrm{x_v}$ is the number of vacancies per formula unit, that is, the number of $(2\mathrm{H})^{\mathrm{x}}_{\mathrm{Mg}}$ or $(4\mathrm{H})^{\mathrm{x}}_{\mathrm{Si}}$ per formula unit.

The assumption that all hydrous vacancies are locally charge balanced, that is, all of the protons are located in the vacant Mg or Si sites (Wright and Catlow 1994; Brodholt and Refson 2000; Braithwaite et al. 2003; Walker et al. 2006, 2007; Umemoto et al. 2011; Crépisson et al. 2014) is made in this calculation. After considering the lattice configurational entropies, the difference in formation energy between $(2\mathrm{H})^{\mathrm{x}}_{\mathrm{Mg}}$ defects and $(4\mathrm{H})^{\mathrm{x}}_{\mathrm{Si}}$ defects in one mole of forsterite is given by

$$\Delta G_{\mathrm{r}}(P,T) = \left[x_{(2\mathrm{H})^{\mathrm{x}}_{\mathrm{Mg}}} N_{\mathrm{A}} G_{\mathrm{r}}^{(2\mathrm{H})^{\mathrm{x}}_{\mathrm{Mg}}} - TS_{\mathrm{conf}}^{(2\mathrm{H})^{\mathrm{x}}_{\mathrm{Mg}}}\right] - \left[x_{(4\mathrm{H})^{\mathrm{x}}_{\mathrm{Si}}} N_{\mathrm{A}} G_{\mathrm{r}}^{(4\mathrm{H})^{\mathrm{x}}_{\mathrm{Si}}} - TS_{\mathrm{conf}}^{(4\mathrm{H})^{\mathrm{x}}_{\mathrm{Si}}}\right] \#(10).$$

Here, $x_{(2\mathrm{H})^{\mathrm{x}}_{\mathrm{Mg}}}$ and $x_{(4\mathrm{H})^{\mathrm{x}}_{\mathrm{Si}}}$ are the concentration of the two hydrous defects, and N_{A} is Avogadro's number. The equation above clearly indicates that the relative stability of these defects depends on defect concentration (water content), temperature, and pressure.

DFT calculations

At the low defect concentrations relevant for the mantle, the probability of interactions between the hydrous defects considered in this paper is small. Therefore, we use a supercell composed of 112 atoms in defect-free forsterite with a single defect as previously used by Umemoto et al. (2011). For the hydrous Mg vacancies reported in previous studies, the lowest-energy configuration consists of two protons bonded to two oxygen ions lying nearly along the O2-O1 edges of a Mg1 vacancy. As there are six oxygen ions per Mg-O polyhedron, there are 15 (${}_6C_2$) possible configurations, not all equivalent, if all the protons are located inside of the Mg1 vacancy, and as one or two protons can point outward of the Mg1 vacancy, there are actually more possibilities. Therefore, a series of different structures were systematically created and optimized to search for possible configurations.

Static calculations for all structures were performed with Local Density Approximation (LDA) (Perdew and Zunger 1981) and Generalized Gradient Approximation (GGA) (Perdew et al. 1996) exchange-correlation functionals using the Quantum-ESPRESSO software (Giannozzi et al. 2009); the plane wave cutoff was chosen to be 544 eV. The pseudopotentials for Si, O and H were generated by Vanderbilt's method (Vanderbilt 1990), and the pseudopotential for Mg was generated by von Barth-Car's method (Dal Corso et al. 1993). The details of GGA pseudopotentials of Si, O, Mg and H are the same as those used in Umemoto et al. (2011), and the LDA pseudopotentials of Si, O and Mg are the same as those used in Umemoto et al. (2008). Brillouin Zone sampling was performed on a displaced $2 \times 2 \times 2$ grid for all supercells. The vibrational density of states (VDOS) for defect free structures were obtained using the

GGA functional using density functional perturbation theory (Baroni et al. 2001). For strongly bonded materials such as oxides and silicate, VDOS and thermodynamics properties obtained from LDA and GGA calculations often are similar, but for structures with hydrous defects, the GGA functional is more appropriate (Umemoto 2010). The dynamical matrices were computed on a $2 \times 2 \times 2$ q-point grid. Obtained force constant matrices were then interpolated on a $6\times 6 \times 6$ q-point gird. The VDOS of the pyroxene and pure olivine are originally from Yu et al. (2008, 2010).

Results

Defect structures

All investigated hydrous defects are presented in Fig. 1 and Tab. 1, listed in order of increasing static energy obtained in GGA level. Nine configurations of $(2\mathrm{H})^{\mathrm{x}}_{\mathrm{Mg}}$ were found based on a systematic search starting from essentially random structures. Configurations 3, 5-8 of $(2\mathrm{H})^{\mathrm{x}}_{\mathrm{Mg}}$ are two-fold degenerate owing to the mirror symmetry plane perpendicular to the *c* axis in defect-free forsterite. The others are non-degenerate. Configurations 1-7 of the $(4\mathrm{H}^{\cdot})^{\mathrm{x}}_{\mathrm{Si}}$ defect were all previously identified (Brodholt and Refson 2000; Walker et al. 2007; Verma and Karki 2009; Umemoto et al. 2011; Xue et al. 2017). Configurations 1, 2, 4 and 6 of $(4\mathrm{H})^{\mathrm{x}}_{\mathrm{Si}}$ are from our previous study (Umemoto et al. 2011), while Configurations 3, 5, 7 of $(4\mathrm{H})^{\mathrm{x}}_{\mathrm{Si}}$ correspond to Configurations 3-5 in Xue et al. (2017). Configurations 2, 3 and 4 of $(4\mathrm{H})^{\mathrm{x}}_{\mathrm{Si}}$ are two-fold degenerate owing to the mirror symmetry plane perpendicular to the *c* axis in defect free forsterite, while the others are non-degenerate. In Configs. 4 and 6, four protons stay close to the surface of the $(4H)_{Si}O_4$ tetrahedron. In Configs. 1 and 2, one proton points away from the $(4H)_{Si}O_4$ tetrahedron; in Configs. 3 and 5, two protons point away from the $(4H)_{Si}O_4$ tetrahedron and in Config. 7 three protons point away from the $(4H)_{Si}O_4$ tetrahedron (Xue et al. 2017). Among all configurations of the $(4\mathrm{H})^{\mathrm{x}}_{\mathrm{Si}}$ defect, the most stable ones are Configs. 1, 2 and 3, consistent with previous studies (Balan et al. 2011; Umemoto et al. 2011; Xue et al. 2017). The energy differences

between other configurations and Config. 1 agree with those in Xue et al. (2017) (see Table 1). Information about the energies, probabilities, and structures of these defects are shown in Table 1 and in the supplementary file. The probabilities of finding configurations in thermodynamic equilibrium at a given temperature are given by $p_i = w_i \exp\left(-\frac{E_i}{k_B T}\right) / \sum_j w_j \exp\left(-\frac{E_j}{k_B T}\right)$, where w_i and E_i are the configurational degeneracy and static energy for the i-th configuration (Brodholt 1997; Walker et al. 2006; Umemoto et al. 2011).

Previous studies indicate that the formation energy of the Mg1 vacancy is 0.54 eV lower than that of the Mg2 vacancy (Brodholt and Refson 2000; Umemoto et al. 2011). Similarly, the formation energy of the hydrous Mg1 defect is lower than that of the hydrous Mg2 defect (Brodholt and Refson 2000; Verma and Karki 2009; Umemoto et al. 2011); thus, we focus here on hydrous Mg1 defects only. Some of the configurations of $(2\mathrm{H})^{\mathrm{x}}_{\mathrm{Mg}}$ were proposed by Walker et al. (2006), including all the configurations with protons connected to two oxygen ions inside or along the edges of the oxygen octahedron. The structure of the lowest-energy configuration of $(2\mathrm{H})^{\mathrm{x}}_{\mathrm{Mg}}$ has two protons bonded to O2 ions, sitting close to the O2-O1 edge of the Mg1 octahedral vacancy. However, the energy difference between this and other structures are somewhat different from those calculated by Walker et al. (2006). This difference is likely caused by the use of different methods, Mott-Littleton method in Walker et al. (2006) and density functional theory in our study. The formation energies of configurations having two protons sitting along the edges or pointing to the interior of the oxygen octahedron are normally lower than configurations containing one or two protons pointing out of the oxygen octahedron. The latter ones have high formation energies and are less probable (see Tab. 1).

The energy differences obtained with LDA are listed in parentheses in Tab. 1. They differ slightly from those obtained with GGA. For example, with LDA, Config. 2 of $(4\mathrm{H})^{\mathrm{x}}_{\mathrm{Si}}$ becomes more stable than Config. 1, but Configs. 1-3 are still the most stable ones. For the $(2\mathrm{H})^{\mathrm{x}}_{\mathrm{Mg}}$ defect, Config. 4 turns into Config. 1

after lattice relaxation with LDA, while with GGA this structure change occurs after 8 GPa. Configuration 5 of $(2\mathrm{H})^{\mathrm{x}}_{\mathrm{Mg}}$ turns into Config. 6 at ~10 GPa and ~12 GPa with LDA and GGA calculations, respectively. Configurations 6 and 2 turn out to be the same after optimization in LDA calculations, while they remain distinct in GGA calculations. These pattern of defect relaxation indicates strong anharmonic effects, with possibly shallow local energy minima in configuration space, and confirms that anharmonic effects can be very sensitive to the choice of exchange-correlation functional when relatively weak bonds are involved (Marcondes et al. 2017).

Substitution of Mg or Si by hydrogens increases the average distance between oxygen ions in the substitutional site and the polyhedron volume. The volumes of regular SiO_4 and $Mg1O_6$ polyhedra are 2.32 and 12.10 Å^3 at 0 GPa and 2.25 and 11.20 Å^3 at 12 GPa, respectively, demonstrating that the volume of SiO_4 and $Mg1O_6$ polyhedra decrease by 3.0% and 7.4%, respectively, as pressure increases to 12 GPa. For all defect configurations, the $(4H)_{Si}O_4$ tetrahedron at 0 GPa is much larger (~40%) and more compressible than the regular SiO_4 tetrahedron. On the one hand, the volume of the defect in Config. 1 changes from 3.27 Å^3 at 0 GPa to 2.85 Å^3 at 12 GPa (volume compressed by 12.8%). On the other hand, the $(2H)_{Mg}O_6$ octahedron is only slightly larger (~4% larger) than that of Mg_1O_6, with its volume changing from 12.58 Å^3 at 0 GPa to 11.01 Å^3 at 12 GPa (volume compressed by 12.5%). Generally, the OH bond length in $(2\mathrm{H})^{\mathrm{x}}_{\mathrm{Mg}}$ is larger than that in $(4\mathrm{H})^{\mathrm{x}}_{\mathrm{Si}}$, and most of these bond-lengths increase with increasing pressure, a sign of hydrogen bond formation with another oxygen across the interstitial site (Umemoto and Wentzcovitch 2004, 2005; Umemoto et al. 2015).

Stability of dominant defects

After computing vibrational free energies and configurational entropies of the two types of hydrous vacancies considered in this study, the difference in formation energies versus water content, temperature, and pressure (Eq. (10)) can be computed. This free energy difference, $\Delta G_{\mathrm{r}}^{\mathrm{LDA}}(P,T)$ and

231 $\Delta G_{\mathrm{r}}^{\mathrm{GGA}}(P,T)$ at 0 and 12 GPa are shown in Fig. 3. It is clear that the formation energy difference and,
232 therefore, the predominance of one defect population over the other, depend on both pressure and
233 temperature. Both LDA and GGA calculations predict that $(2\mathrm{H})_{\mathrm{Mg}}^{\mathrm{x}}$ defects dominate at high
234 temperatures, while $(4\mathrm{H})_{\mathrm{Si}}^{\mathrm{x}}$ defects dominate at ambient temperature. For instance, at a typical upper
235 mantle pressure and temperature (12 GPa and 1700K), the hydrous Mg defect is more stable. The key to
236 this high-temperature stabilization is the configurational entropy.

237 # Discussion

238 To investigate the origin of the relative stability of these two defects at different pressures and
239 temperatures, we recalculated the free energy difference (Eq. 10) by examining the effect of various
240 terms contributing to the free energy difference at GGA level. First, Fig. 3 clearly indicates that by
241 increasing pressure the stability field of the hydrous Si defect is extended to higher temperatures. This
242 pressure effect is best investigated at zero Kelvin. In Fig. 4, the enthalpy difference $\Delta G_{\mathrm{r}}^{\mathrm{GGA}}(P,0) =$
243 $\Delta H_{\mathrm{r}}(P,0)$ and the contribution of $P\Delta V_{\mathrm{r}}(P)$ to ΔH_{r} are plotted as a function of pressure. The stability of
244 the $(4\mathrm{H})_{\mathrm{Si}}^{\mathrm{x}}$ defect increases with increasing pressure primarily because this defect is more compressive
245 than the hydrous Mg defect, as noted above. Therefore, it is clearly very important to obtain the correct
246 pressure dependences for these defect structures.

247 The stabilization of the $(2\mathrm{H})_{\mathrm{Mg}}^{\mathrm{x}}$ defect with increasing temperature is easier to understand. This defect
248 is stabilized by entropy; but, as indicated above, there are several contributions to the configurational
249 entropy, including the lattice configurational entropy and the entropy caused by different internal
250 configurations of certain hydrous defect. The latter can be investigated by considering different
251 numbers of $(2\mathrm{H})_{\mathrm{Mg}}^{\mathrm{x}}$ and $(4\mathrm{H})_{\mathrm{Si}}^{\mathrm{x}}$ defects separately.

Effects of internal configuration entropy of $(2\mathrm{H})^{\mathrm{x}}_{\mathrm{Mg}}$ and $(4\mathrm{H})^{\mathrm{x}}_{\mathrm{Si}}$ defects are illustrated in Figs. 5 (a) and (b), respectively, as plots of temperature versus water content. Below (above) the line the free energy difference favors $(4\mathrm{H})^{\mathrm{x}}_{\mathrm{Si}}$ defects ($(2\mathrm{H})^{\mathrm{x}}_{\mathrm{Mg}}$ defects. In Fig. 5 (a), the relative stability of $(2\mathrm{H})^{\mathrm{x}}_{\mathrm{Mg}}$ defect increases by increasing the number of $(2\mathrm{H})^{\mathrm{x}}_{\mathrm{Mg}}$ configurations considered, but changes little when the number of configurations exceeds seven. This result can be explained by the probabilities of these configurations (Tab. 1). The probabilities of Configs. 8-9 are negligible even at high temperature due to their high formation energies. A similar trend is also observed for $(4\mathrm{H})^{\mathrm{x}}_{\mathrm{Si}}$ defect configurations. The stability of this type of defect changes little when these low probability configurations are included. The most influential configurations are those with low energy and high probability. Therefore, taking more configurations with larger formation energies of $(2\mathrm{H})^{\mathrm{x}}_{\mathrm{Mg}}$ and $(4\mathrm{H})^{\mathrm{x}}_{\mathrm{Si}}$ defects will not change further their relative stability. Figure 5 indicates that nine configurations of $(2\mathrm{H})^{\mathrm{x}}_{\mathrm{Mg}}$ and seven configurations of $(4\mathrm{H})^{\mathrm{x}}_{\mathrm{Si}}$ defects are sufficient to investigate the relative stability of these two defect types. This result clearly points to the importance of proper identification and sampling of possible defect configurations in these calculations.

The impact of various entropy sources on the formation energy difference of these two hydrous defects is illustrated in Fig. 6 as function of temperature and water content. Figures 6 (a) and 6 (b) include contributions from the internal configurational entropy for variable numbers of defect configurations in each site and exclude contributions from vibrational (entropic or enthalpic) free energy, G_{vib}, as well as "mixing" free energy, $G_{mix} = - TS_{conf}$, where S_{conf} is given by Eq. (9). These figures indicate how the relative stability of these defects varies with the number of configurations identified. In particular, the $(4\mathrm{H})^{\mathrm{x}}_{\mathrm{Si}}$ defect stability can be overestimated if an insufficient number of $(2\mathrm{H})^{\mathrm{x}}_{\mathrm{Mg}}$ defect configurations is included. Figures 6 (c) and 6 (d) demonstrate that inclusion of vibrational effects further stabilize the $(2\mathrm{H})^{\mathrm{x}}_{\mathrm{Mg}}$ relative to the $(4\mathrm{H})^{\mathrm{x}}_{\mathrm{Si}}$ defect. This effect is due to the lower frequency of O-H vibrational modes

in the $(2\mathrm{H})^{\mathrm{x}}_{\mathrm{Mg}}$ (see Fig. 2). Figures 6(e) and 6(f) indicate that the $(2\mathrm{H})^{\mathrm{x}}_{\mathrm{Mg}}$ defect stability increases to a greater extent when the contribution of lattice configuration entropy (G_{mix}) is include. For nearly the same water content, the number of $(4\mathrm{H})^{\mathrm{x}}_{\mathrm{Si}}$ defects is half the number of $(2\mathrm{H})^{\mathrm{x}}_{\mathrm{Mg}}$ defects, and, therefore, the $(4\mathrm{H})^{\mathrm{x}}_{\mathrm{Si}}$ defects contribute less entropy resulting in the destabilization of $(4\mathrm{H})^{\mathrm{x}}_{\mathrm{Si}}$ at higher temperatures. This effect is clearly dependent of water content in the range of water concentration expected in natural olivine samples, that is, less than 1000 ppmw (Bolfan-Casanova, 2005). A comparison between the diagrams presented in Fig. 5 (a-b) and Fig 6 (a-f) provides a clear indication of the necessity to include all internal defect configurations, G_{mix}, and G_{vib} simultaneously in these calculations. This conclusion is general and applies to all hydrous defects in nominally anhydrous minerals. The results discussed above clearly point out the increase stability of the $(2\mathrm{H})^{\mathrm{x}}_{\mathrm{Mg}}$ defect with increasing temperature.

Our results correspond to situations where thermodynamic equilibrium can be achieved in the presence of enstatite. As pointed out earlier (Walker et al. 2007), the relative stability of these defects depends on the nature of co-existing phases. However, the increased stability of the $(2\mathrm{H})^{\mathrm{x}}_{\mathrm{Mg}}$ defect with increasing temperature is independent of the co-existing phase. This situation is primarily due to the lattice configuration entropy effect. Here we emphasize that the internal configuration entropy of these defects also affects their relative stability. It is not a trivial exercise to identify all of them and calculations need to be approximate. Besides, as pointed out above, *ab initio* calculations have systematic errors that are not easily accessible and anharmonic effects might be important as well. Also, one can easily imagine other defect states not addressed here, for example, similar Mg2 defects, interstitial protons, etc. For instance, $\left\{(3\mathrm{H})^{/}_{\mathrm{Si}} + \mathrm{H}^{\cdot}_{\mathrm{i}}\right\}^{\mathrm{x}}$, i.e., three protons in the Si vacancy and one proton in the interstitial site, or similarly $\left\{(\mathrm{H})^{/}_{\mathrm{Mg}} + \mathrm{H}^{\cdot}_{\mathrm{i}}\right\}^{\mathrm{x}}$, have much larger entropy owing to the large number of configurations available for interstitial protons. The free energy of these defects should also

be carefully investigated for obtaining a full picture of their relative stability. Therefore, direct comparison of these results with experimental observations can be subtle and difficult.

Implications

Despite these uncertainties, some implications seem warranted. The destabilization of $(4\mathrm{H})_{\mathrm{Si}}^{\mathrm{x}}$ with respect to the $(2\mathrm{H})_{\mathrm{Mg}}^{\mathrm{x}}$defect with increasing temperature, as shown in Fig. 3, should produce changes in experimental IR spectra if equilibrium conditions are achieved. Similarly, the populations of different $(4\mathrm{H})_{\mathrm{Si}}^{\mathrm{x}}$ or $(2\mathrm{H})_{\mathrm{Mg}}^{\mathrm{x}}$ defects also depend on temperature (see Table 1) and could equally well produce changes in IR spectra. The precise temperature at which such spectral changes should manifest is difficult to predict accurately given the factors mentioned above. Nevertheless, our results might apply to explain a notable change in the IR spectrum of hydrous olivine, that is, a reversible change in intensity of the 3612 cm^{-1} peak, upon heating and cooling (Yang and Keppler, 2011). This prominent low-temperature band is thought to belong to the $(4\mathrm{H})_{\mathrm{Si}}^{\mathrm{x}}$ group, confirming our observation that equilibrium between different types of hydrous defects are temperature-dependent. This band involves the coupled stretching of the four OH^- groups of one particular $(4\mathrm{H})_{\mathrm{Si}}^{\mathrm{x}}$ configuration and suggests that a change in the defect geometry with temperature might explain the change of IR band without requiring proton migration or a change in the nature of the hydrous defect (Balan et al. 2017). Indeed, even within the quasi harmonic approximation (QHA), results presented in Table 1 suggest that the probability of different $(4\mathrm{H})_{\mathrm{Si}}^{\mathrm{x}}$ defect configurations can vary considerably within the temperature range of Yang and Keppler's experiment. For example, while the most stable configuration of $(4\mathrm{H})_{\mathrm{Si}}^{\mathrm{x}}$ defect is marginally more likely at 300 K, the second most stable configuration is more likely at 1500 K. While probabilities shown in Table 1 might carry significant uncertainties, this type of result is consistent with the proposal of Balan et al. (2017). This possibility should be addressed in the future with anharmonic calculations of the IR spectra of these different defect configurations.

Our calculations indicate that water speciation in olivine is influenced by temperature and pressure, in addition to the well-known influence of the surroundings. As mantle properties may be affected by the speciation of water in olivine, application of experimental results to the mantle should account for these water speciation dependencies.

Acknowledgments

This work was supported by NSF/EAR grant 1161023. Computations were performed at the Minnesota Supercomputing Institute and at the Texas Advanced Computing Center (Stampede2) under an XSEDE allocation. We thank the Editor, Roland Stalder, and two anonymous reviewers for their constrictive comments that helped improve the clarity of the manuscript.

References

Bai, Q., and Kohlstedt, D.L. (1992) Substantial hydrogen solubility in olivine and implications for water storage in the mantle. Nature, 357, 672–674.

Bai, Q., and Kohlstedt, D.L. (1993) Effects of chemical environment on the solubility and incorporation mechanism for hydrogen in olivine. Physics and Chemistry of Minerals, 19, 460–471.

Balan, E., Ingrin, J., Delattre, S., Kovács, I., and Blanchard, M. (2011) Theoretical infrared spectrum of OH-defects in forsterite. European Journal of Mineralogy, 23, 285–292.

Balan, E., Blanchard, M., Lazzeri, M., and Ingrin, J. (2014) Contribution of interstitial OH groups to the incorporation of water in forsterite. Physics and Chemistry of Minerals, 41, 105–114.

——— (2017) Theoretical Raman spectrum and anharmonicity of tetrahedral OH defects in hydrous forsterite. European Journal of Mineralogy, 29, 201–212.

Baroni, S., De Gironcoli, S., Dal Corso, A., and Giannozzi, P. (2001) Phonons and related crystal properties

342 from density-functional perturbation theory. Reviews of Modern Physics, 73, 515–562.

343 Bell, D.R., and Rossman, G.R. (1992) Water in Earth's Mantle: The Role of Nominally Anhydrous Minerals.
344 Science, 255, 1391–1397.

345 Berry, A.J., Hermann, J., O'Neill, H.S.C., and Foran, G.J. (2005) Fingerprinting the water site in mantle
346 olivine. Geology, 33, 869.

347 Blanchard, M., Ingrin, J., Balan, E., Kovács, I., and Withers, A.C. (2017) Effect of iron and trivalent cations
348 on OH defects in olivine. American Mineralogist, 102, 302–311.

349 Bolfan-Casanova, N. (2005) Water in the Earth's mantle. Mineralogical Magazine, 69, 229–258.

350 Bolfan-Casanova, N., Montagnac, G., and Reynard, B. (2014) Measurement of water contents in olivine
351 using Raman spectroscopy. American Mineralogist, 99, 149–156.

352 Braithwaite, J.S., Sushko, P. V., Wright, K., and Catlow, C.R.A. (2002) Hydrogen defects in Forsterite: A
353 test case for the embedded cluster method. The Journal of Chemical Physics, 116, 2628–2635.

354 Braithwaite, J.S., Wright, K., and Catlow, C.R.A. (2003) A theoretical study of the energetics and IR
355 frequencies of hydroxyl defects in forsterite. Journal of Geophysical Research: Solid Earth, 108,
356 2284.

357 Brodholt, J. (1997) Ab initio calculations on point defects in forsterite (Mg 2 SiO 4) and implications for
358 diffusion and creep, 82, 1049–1053.

359 Brodholt, J.P., and Refson, K. (2000) An ab initio study of hydrogen in forsterite and a possible
360 mechanism for hydrolytic weakening. Journal of Geophysical Research: Solid Earth, 105, 18977–
361 18982.

362 Carter, N.L., and Ave'lallemant, H.G. (1970) High Temperature Flow of Dunite and Peridotite.

(Intergovernmental Panel on Climate Change, Ed.)Geological Society of America Bulletin, 81, 2181.

Chopra, P.N., and Paterson, M.S. (1984) The role of water in the deformation of dunite. Journal of Geophysical Research: Solid Earth, 89, 7861–7876.

Crépisson, C., Bureau, H., Blanchard, M., Ingrin, J., and Balan, E. (2014) Theoretical infrared spectrum of partially protonated cationic vacancies in forsterite. European Journal of Mineralogy, 26, 203–210.

Dal Corso, A., Baroni, S., Resta, R., and de Gironcoli, S. (1993) Ab initio calculation of phonon dispersions in II-VI semiconductors. Physical Review B, 47, 3588.

Demouchy, S., and Mackwell, S. (2003) Water diffusion in synthetic iron-free forsterite. Physics and Chemistry of Minerals, 30, 486–494.

Giannozzi, P., Baroni, S., Bonini, N., Calandra, M., Car, R., Cavazzoni, C., Ceresoli, D., Chiarotti, G.L., Cococcioni, M., Dabo, I., and others (2009) QUANTUM ESPRESSO: a modular and open-source software project for quantum simulations of materials. Journal of Physics: Condensed Matter, 21, 395502.

Green, D.H. (1973) Experimental melting studies on a model upper mantle composition at high pressure under water-saturated and water-undersaturated conditions. Earth and Planetary Science Letters, 19, 37–53.

Haiber, M., Ballone, P., and Parrinello, M. (1997) Structure and dynamics of protonated Mg2SiO4: An ab-initio molecular dynamics study. American Mineralogist, 82, 913–922.

Hirose, K. (1997) Melting experiments on Iherzolite KLB-1 under hydrous conditions and generation of high-magnesian andesitic melts. Geology, 25, 42–44.

Hirschmann, M., and Kohlstedt, D. (2012) Water in Earth's mantle. Physics Today, 65, 40.

384 Hushur, A., Manghnani, M.H., Smyth, J.R., Nestola, F., and Frost, D.J. (2009) Crystal chemistry of hydrous
385 forsterite and its vibrational properties up to 41 GPa. American Mineralogist, 94, 751–760.

386 Ingrin, J., Liu, J., Depecker, C., Kohn, S.C., Balan, E., and Grant, K.J. (2013) Low-temperature evolution of
387 OH bands in synthetic forsterite, implication for the nature of H defects at high pressure. Physics
388 and Chemistry of Minerals, 40, 499–510.

389 Karato, S. (1990) The role of hydrogen in the electrical conductivity of the upper mantle. Nature, 347,
390 272–273.

391 Karato, S.-I., Paterson, M.S., and FitzGerald, J.D. (1986) Rheology of synthetic olivine aggregates:
392 Influence of grain size and water. Journal of Geophysical Research, 91, 8151.

393 Kohlstedt, D.L., and Mackwell, S.J. (1998) Diffusion of Hydrogen and Intrinsic Point Defects in Olivine.
394 Zeitschrift für Physikalische Chemie, 207, 147–162.

395 Kohlstedt, D.L., Keppler, H., and Rubie, D.C. (1996) Solubility of water in the α, β and γ phases of (Mg,Fe)
396 2 SiO 4. Contributions to Mineralogy and Petrology, 123, 345–357.

397 Kohn, S.C. (1996) Solubility of H20 in nominally anhydrous mantle minerals using IH MAS NMR.
398 American Mineralogist, 81, 1523–1526.

399 Kovács, I., O'nelll, H.S.C., Hermann, J., and Hauri, E.H. (2010) Site-specific infrared O-H absorption
400 coefficients for water substitution into olivine. American Mineralogist, 95, 292–299.

401 Kröger, F.A., and Vink, H.J. (1956) Relations between the Concentrations of Imperfections in Crystalline
402 Solids pp. 307–435.

403 Kudoh, Y., Kuribayashi, T., Kagi, H., and Inoue, T. (2006) Cation vacancy and possible hydrogen positions
404 in hydrous forsterite, Mg1.985Si0.993H0.06O4, synthesized at 13.5 GPa and 1300 °C. Journal of

405 Mineralogical and Petrological Sciences, 101, 265–269.

406 Kushiro, I. (1972) Effect of Water on the Composition of Magmas Formed at High Pressures. Journal of
407 Petrology, 13, 311–334.

408 Lemaire, C., Kohn, S.C., and Brooker, R. a. (2004) The effect of silica activity on the incorporation
409 mechanisms of water in synthetic forsterite: A polarised infrared spectroscopic study.
410 Contributions to Mineralogy and Petrology, 147, 48–57.

411 Marcondes, M.L., Wentzcovitch, R.M., and Assali, L.V.C. (2017) Importance of van der Waals interaction
412 on structural, vibrational, and thermodynamics properties of NaCl. Solid State Sciences, 11, 1343–
413 1349.

414 Martin, R.F., and Donnay, G. (1972) Hydroxyl in the mantle. American Mineralogist, 57, 554–570.

415 Matveev, S., O'Neill, H.S.C., Ballhaus, C., Taylor, W.R., and Green, D.H. (2001) Effect of Silica Activity on
416 OH- IR Spectra of Olivine: Implications for Low-aSiO2 Mantle Metasomatism. Journal of Petrology,
417 42, 721–729.

418 Mei, S., and Kohlstedt, D.L. (2000a) Influence of water on plastic deformation of olivine aggregates: 1.
419 Diffusion creep regime. Journal of Geophysical Research: Solid Earth, 105, 21457–21469.

420 ——— (2000b) Influence of water on plastic deformation of olivine aggregates: 2. Dislocation creep
421 regime. Journal of Geophysical Research: Solid Earth, 105, 21471–21481.

422 Nishi, M., Irifune, T., Tsuchiya, J., Tange, Y., Nishihara, Y., Fujino, K., and Higo, Y. (2014) Stability of
423 hydrous silicate at high pressures and water transport to the deep lower mantle. Nature
424 Geoscience, 7, 224–227.

425 Ohtani, E. (2005) Water in the Mantle. Elements, 1, 25–30.

426 Otsuka, K., and Karato, S. (2011) Control of the water fugacity at high pressures and temperatures:
427 Applications to the incorporation mechanisms of water in olivine. Physics of the Earth and
428 Planetary Interiors, 189, 27–33.

429 Peacock, S.A. (1990) Fluid Processes in Subduction Zones. Science, 248, 329–337.

430 Pearson, D.G., Brenker, F.E., Nestola, F., McNeill, J., Nasdala, L., Hutchison, M.T., Matveev, S., Mather, K.,
431 Silversmit, G., Schmitz, S., and others (2014) Hydrous mantle transition zone indicated by
432 ringwoodite included within diamond. Nature, 507, 221–224.

433 Perdew, J.P., and Zunger, A. (1981) Self-interaction correction to density-functional approximations for
434 many-electron systems. Physical Review B, 23, 5048.

435 Perdew, J.P., Burke, K., and Ernzerhof, M. (1996) Generalized Gradient Approximation Made Simple.
436 Physical Review Letters, 77, 3865–3868.

437 Rubey, W.W. (1951) Geologic history of sea water An attempt to state the problem. GSA Bulletin, 62,
438 1111–1148.

439 Shukla, G., and Wentzcovitch, R.M. (2016) Spin crossover in (Mg,Fe3+)(Si,Fe3+)O3 bridgmanite: Effects
440 of disorder, iron concentration, and temperature. Physics of the Earth and Planetary Interiors, 260,
441 53–61.

442 Smyth, J.R. (1994) A crystallographic model for hydrous wadsleyite (beta-Mg2 SiO4); an ocean in the
443 Earth's interior? American Mineralogist, 79, 1021–1024.

444 Smyth, J.R., Frost, D.J., Nestola, F., Holl, C.M., and Bromiley, G. (2006) Olivine hydration in the deep
445 upper mantle: Effects of temperature and silica activity. Geophysical Research Letters, 33, 1–5.

446 Tollan, P.M.E., Smith, R., O'Neill, H.S.C., and Hermann, J. (2017) The responses of the four main

substitution mechanisms of H in olivine to H2O activity at 1050 °C and 3 GPa. Progress in Earth and Planetary Science, 4, 14.

Umemoto, K. (2010) Computer Simulations on Phase Transitions in Ice. Reviews in Mineralogy and Geochemistry, 71, 315–335.

Umemoto, K., and Wentzcovitch, R.M. (2004) Amorphization in quenched ice VIII: A first-principles study. Physical Review B, 69, 180103.

——— (2005) Theoretical study of the isostructural transformation in ice VIII. Physical Review B, 71, 12102.

Umemoto, K., Wentzcovitch, R.M., Yu, Y.G., and Requist, R. (2008) Spin transition in (Mg,Fe)SiO3 perovskite under pressure. Earth and Planetary Science Letters, 276, 198–206.

Umemoto, K., Wentzcovitch, R.M., De Gironcoli, S., and Baroni, S. (2010) Order-disorder phase boundary between ice VII and VIII obtained by first principles. Chemical Physics Letters, 499, 236–240.

Umemoto, K., Wentzcovitch, R.M., Hirschmann, M.M., Kohlstedt, D.L., and Withers, A.C. (2011) A first-principles investigation of hydrous defects and IR frequencies in forsterite: The case for Si vacancies. American Mineralogist, 96, 1475–1479.

Umemoto, K., Sugimura, E., de Gironcoli, S., Nakajima, Y., Hirose, K., Ohishi, Y., and Wentzcovitch, R.M. (2015) Nature of the Volume Isotope Effect in Ice. Physical Review Letters, 115, 173005.

van Keken, P.E., Hacker, B.R., Syracuse, E.M., and Abers, G.A. (2011) Subduction factory: 4. Depth-dependent flux of H2O from subducting slabs worldwide. Journal of Geophysical Research, 116, B01401.

Vanderbilt, D. (1990) Soft self-consistent pseudopotentials in a generalized eigenvalue formalism.

468 Physical Review B, 41, 7892.

469 Verma, A.K., and Karki, B.B. (2009) Ab initio investigations of native and protonic point defects in
470 Mg_2SiO_4 polymorphs under high pressure. Earth and Planetary Science Letters, 285, 140–149.

471 Walker, A.M., Demouchy, S., and Wright, K. (2006) Computer modelling of the energies and vibrational
472 properties of hydroxyl groups in α- and β-Mg2SiO4. European Journal of Mineralogy, 18, 529–543.

473 Walker, a. M., Hermann, J., Berry, a. J., and O'Neill, H.S.C. (2007) Three water sites in upper mantle
474 olivine and the role of titanium in the water weakening mechanism. Journal of Geophysical
475 Research, 112, B05211.

476 Wang, D., Mookherjee, M., Xu, Y., and Karato, S. (2006) The effect of water on the electrical conductivity
477 of olivine. Nature, 443, 977–980.

478 Wright, K., and Catlow, C.R.A. (1994) A computer simulation study of (OH) defects in olivine. Physics and
479 Chemistry of Minerals, 20, 515–518.

480 Xue, X., Kanzaki, M., Turner, D., and Loroch, D. (2017) Hydrogen incorporation mechanisms in forsterite:
481 New insights from 1 H and 29 Si NMR spectroscopy and first-principles calculation. American
482 Mineralogist, 102, 519–536.

483 Yang, X. -z., and Keppler, H. (2011) In-situ infrared spectra of OH in olivine to 1100 C. American
484 Mineralogist, 96, 451–454.

485 Yoshino, T., and Katsura, T. (2013) Electrical Conductivity of Mantle Minerals: Role of Water in
486 Conductivity Anomalies. Annual Review of Earth and Planetary Sciences, 41, 605–628.

487 Yu, Y.G., Wu, Z., and Wentzcovitch, R.M. (2008) α–β–γ transformations in Mg2SiO4 in Earth's transition
488 zone. Earth and Planetary Science Letters, 273, 115–122.

489 Yu, Y.G., Wentzcovitch, R.M., and Angel, R.J. (2010) First principles study of thermodynamics and phase
490 transition in low-pressure (P21/c) and high-pressure (C2/c) clinoenstatite MgSiO3. Journal of
491 Geophysical Research: Solid Earth, 115, 1–10.

492

493

Captions

Figure 1 – Configurations of $(4\mathrm{H})_{\mathrm{Si}}^{\mathrm{x}}$ and $(2\mathrm{H})_{\mathrm{Mg}}^{\mathrm{x}}$ defects. Red and white spheres represent oxygen ions and protons, respectively. Pink and green polyhedra represent vacant Si and Mg sites. Configurations 1, 2, 4 and 6 of $(4\mathrm{H})_{\mathrm{Si}}^{\mathrm{x}}$ and Config. 1 of $(2\mathrm{H})_{\mathrm{Mg}}^{\mathrm{x}}$ are from Umemoto et al. (2011). Configurations 3, 5 and 7 of $(4\mathrm{H})_{\mathrm{Si}}^{\mathrm{x}}$ are from Xue et al. (2017), with the fourth hydrogen in configuration 7 existing just beneath O1. Configurations 1-6 and 8 of $(2\mathrm{H})_{\mathrm{Mg}}^{\mathrm{x}}$ were described in the Walker et al. (2006).

Figure 2 – Vibrational density of states (VDOS) at GGA level for a $2 \times 1 \times 2$ supercell of forsterite at 0 GPa (see text for q point sampling). Black, red, and blue correspond to defect free, one $(2\mathrm{H})_{\mathrm{Mg}}^{\mathrm{x}}$, and one $(4\mathrm{H})_{\mathrm{Si}}^{\mathrm{x}}$ defect configurations, respectively.

Figure 3 – Gibbs free energy difference between the two hydrous defects considered in this study, $\Delta G_{\mathrm{r}}^{\mathrm{LDA,GGA}}(P,T)$ given by Eq. (10), in temperature – water concentration space at **(a)** LDA result at 0 GPa and **(b)** GGA result at 0 GPa; **(c)** LDA result at 12 GPa and **(d)** GGA result at 12 GPa. $(2\mathrm{H})_{\mathrm{Mg}}^{\mathrm{x}}$ is more (less) stable than $(4\mathrm{H})_{\mathrm{Si}}^{\mathrm{x}}$ defects in the red (blue) regions. The total number of distinct $(2\mathrm{H})_{\mathrm{Mg}}^{\mathrm{x}}$ and $(4\mathrm{H})_{\mathrm{Si}}^{\mathrm{x}}$ configurations considered in this study are 9 and 7, respectively. The solid line denotes the boundary between the red and blue regions, that is, $\Delta G_{\mathrm{r}}(P,T) = 0$.

Figure 4 – Enthalpy difference, $\Delta H_r(P,0) = 2H_{\mathrm{r}}^{(2\mathrm{H})_{\mathrm{Mg}}^{\mathrm{x}}} - H_{\mathrm{r}}^{(4\mathrm{H})_{\mathrm{Si}}^{\mathrm{x}}}$ or $\Delta H_r(P,0) = \Delta E_{\mathrm{r}}(P) + P\Delta V_{\mathrm{r}}(P)$, and $P\Delta V_{\mathrm{r}}(P)$ obtained from Eqs. (3) and (4) at 0 K (static calculation) plotted versus pressure.

515 **Figure 5** - $\Delta G_r^{\mathrm{GGA}}(P,T) = 0$ (see Eq. (10)) at 12 GPa including different internal configuration energy
516 contributions plotted parametrically in temperature – water content space. In **(a)** various numbers of
517 distinct $(2\mathrm{H})^{\mathrm{x}}_{\mathrm{Mg}}$ configurations and 7 distinct $(4\mathrm{H})^{\mathrm{x}}_{\mathrm{Si}}$ configurations are considered, while in **(b)** 9
518 $(2\mathrm{H})^{\mathrm{x}}_{\mathrm{Mg}}$ and various numbers of $(4\mathrm{H})^{\mathrm{x}}_{\mathrm{Si}}$ distinct configurations are considered. The ratio of the number
519 of distinct configurations, $\#(2\mathrm{H})^{\mathrm{x}}_{\mathrm{Mg}}$: $\#(4\mathrm{H})^{\mathrm{x}}_{\mathrm{Si}}$, are shown in the legend.

520

521 **Figure 6** – Plots of $\Delta G_r^{\mathrm{GGA}}(P,T) = 0$ (see Eq. (10)) at 12 GPa including different energy contributions in
522 temperature – water concentration space: **(a)** and **(b)** exclude G_{vib} and G_{mix}, **(c)** and **(d)** include G_{vib} and
523 exclude G_{mix}, **(e)** and **(f)** exclude G_{vib} and include G_{mix}. The ratios of the number of configurations,
524 $\#(2\mathrm{H})^{\mathrm{x}}_{\mathrm{Mg}}$: $\#(4\mathrm{H})^{\mathrm{x}}_{\mathrm{Si}}$ are shown in the legend in each plot.

525

526

Tables

Table 1. Degeneracies, relative energies, and probabilities, $p_i = w_i \exp\left(-\frac{E_i}{k_B T}\right) / \sum_j w_j \exp\left(-\frac{E_j}{k_B T}\right)$, of various defects (static calculation). Numbers outside (inside) parentheses correspond to PBE-GGA (LDA) results.

$(4\mathrm{H})^{\mathrm{x}}_{\mathrm{Si}}$	Degeneracy	$E_{Conf.x} - E_{Conf.1}$ (eV)	Probability (300K)	Probability (1500K)
Conf. 1	1	0.00 (0.00)	0.497 (0.186)	0.225 (0.199)
Conf. 2	2	0.02 (-0.02)	0.458 (0.806)	0.386 (0.465)
Conf. 3	2	0.08 (0.10)	0.045 (0.008)	0.243 (0.184)
Conf. 4	2	0.23 (0.21)	0.000 (0.000)	0.076 (0.078)
Conf.5	1	0.23 (0.27)	0.000 (0.000)	0.038 (0.025)
Conf.6	1	0.33 (0.20)	0.000 (0.000)	0.018 (0.042)
Conf.7	1	0.36 (0.45)	0.000 (0.000)	0.014 (0.006)
$(2\mathrm{H})^{\mathrm{x}}_{\mathrm{Mg}}$				
Conf. 1	1	0.00 (0.00)	0.996 (0.500)	0.603 (0.417)
Conf. 2	1	0.14 (0.24)	0.004 (0.000)	0.204 (0.065)
Conf. 3	2	0.29 (0.33)	0.000 (0.000)	0.128 (0.065)
Conf. 4	1	0.48 (0.00)	0.000 (0.500)	0.015 (0.417)
Conf. 5	2	0.52 (0.58)	0.000 (0.000)	0.022 (0.009)
Conf. 6	2	0.54 (0.55)	0.000 (0.000)	0.018 (0.012)
Conf. 7	2	0.63 (0.73)	0.000 (0.000)	0.009 (0.003)
Conf. 8	2	0.89 (0.55)	0.000 (0.000)	0.001 (0.012)
Conf. 9	1	0.93 (1.01)	0.000 (0.000)	0.000 (0.000)

Figures

Figure 1

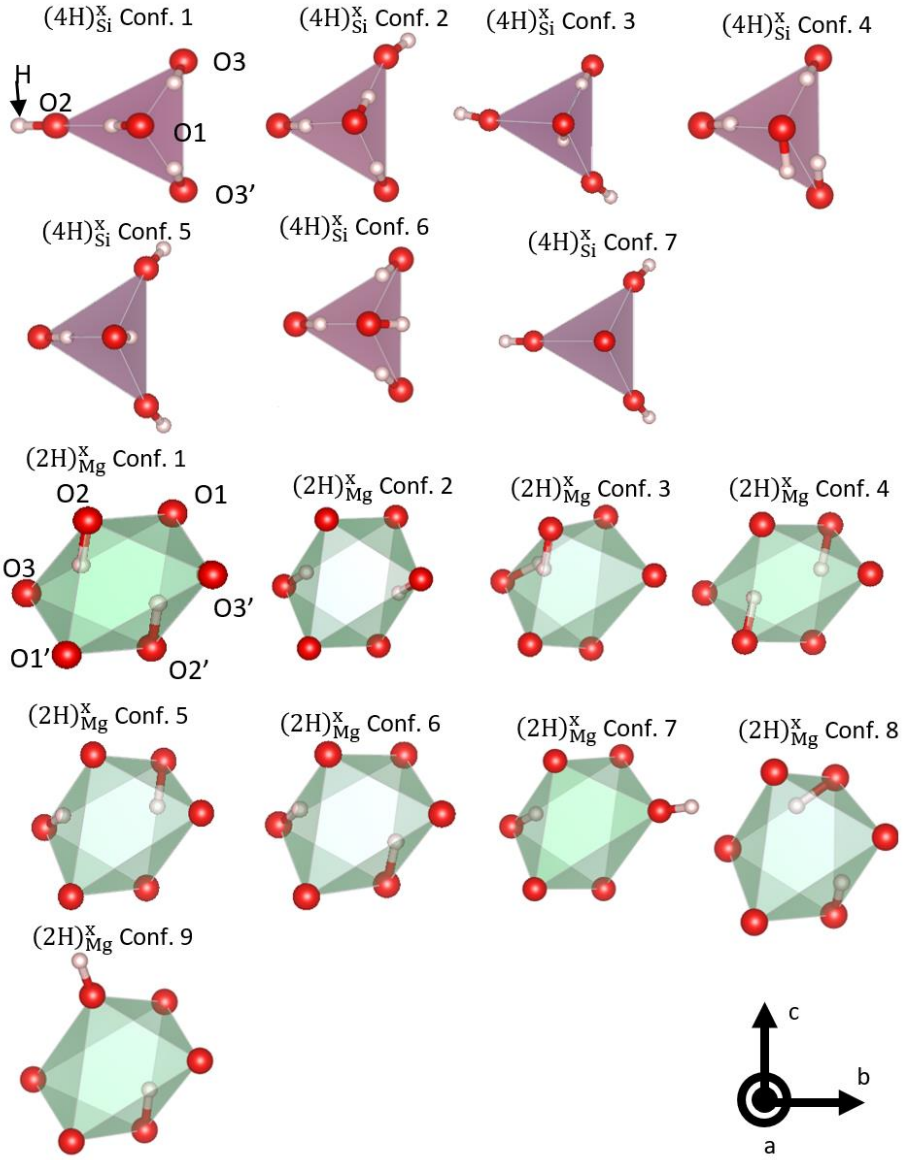

536 **Figure 2**

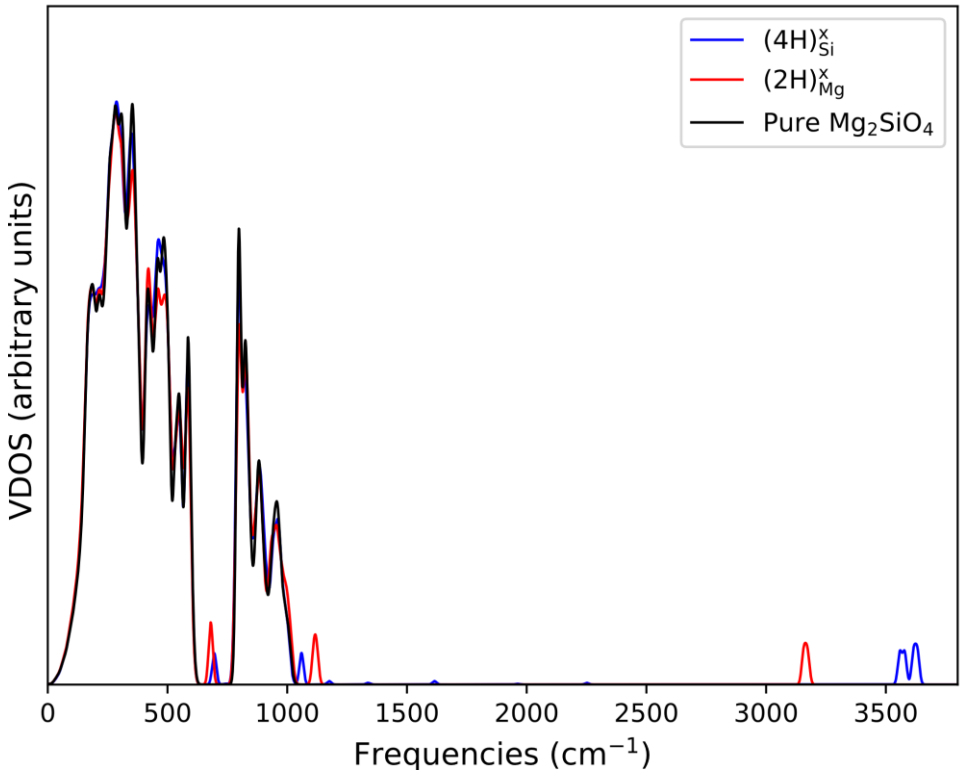

537

538

539

Figure 3

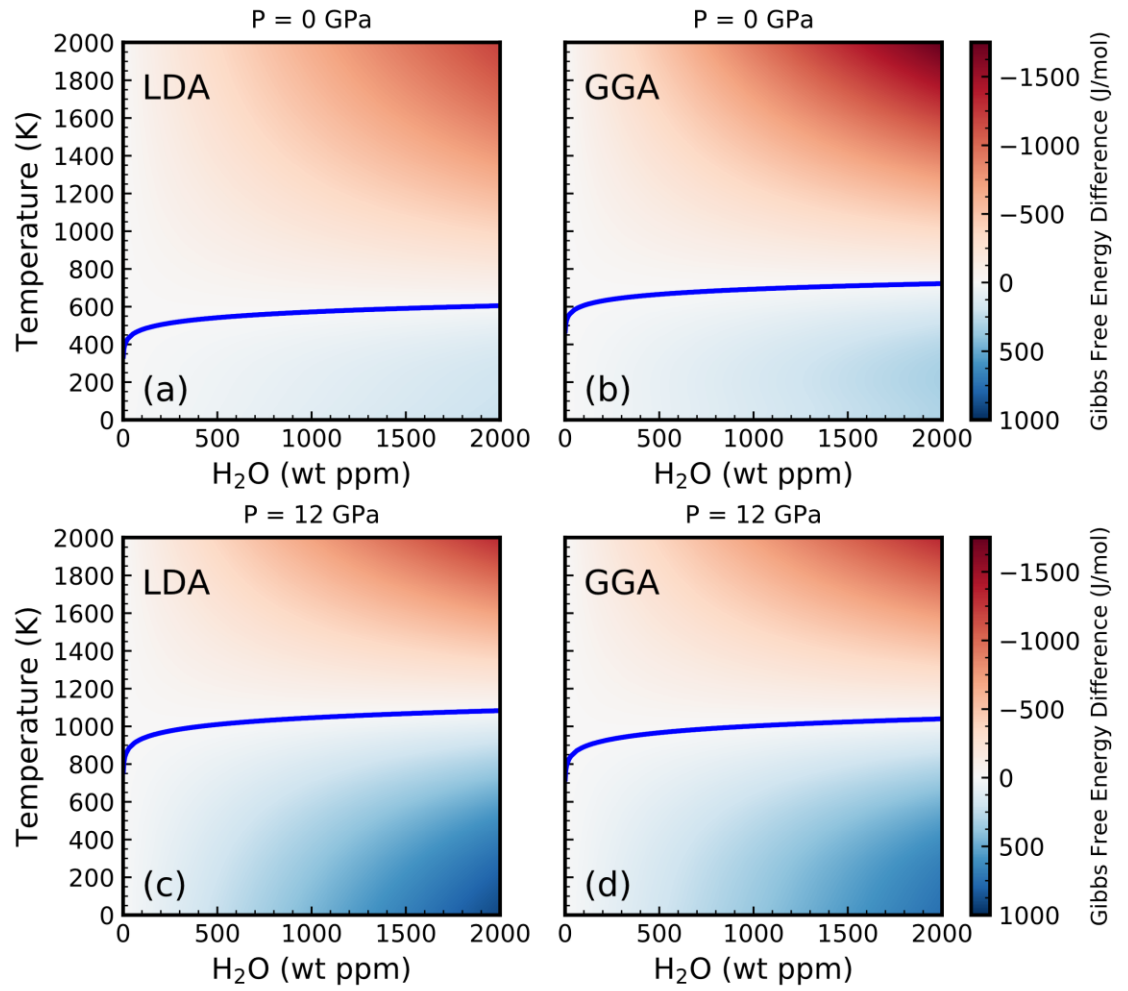
P = 0 GPa
LDA
(a)
P = 0 GPa
GGA
(b)
P = 12 GPa
LDA
(c)
P = 12 GPa
GGA
(d)
Temperature (K)
H2O (wt ppm)
Gibbs Free Energy Difference (J/mol)
0
200
400
600
800
1000
1200
1400
1600
1800
2000
500
1000
1500
−1500
−1000
−500
0
500
1000

543 **Figure 4**

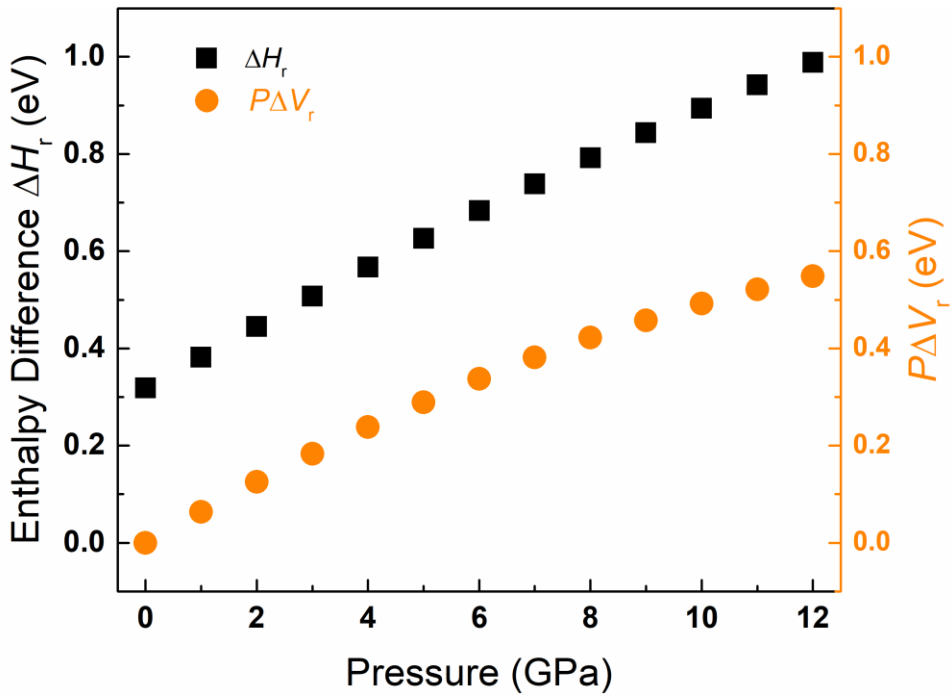

544

545

546 **Figure 5**

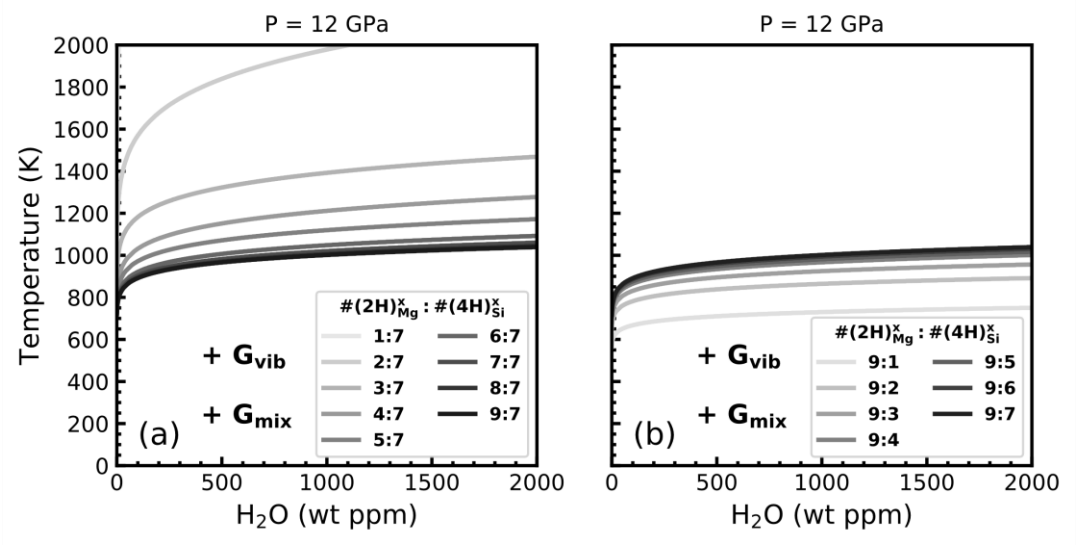

547

548

549 **Figure 6**

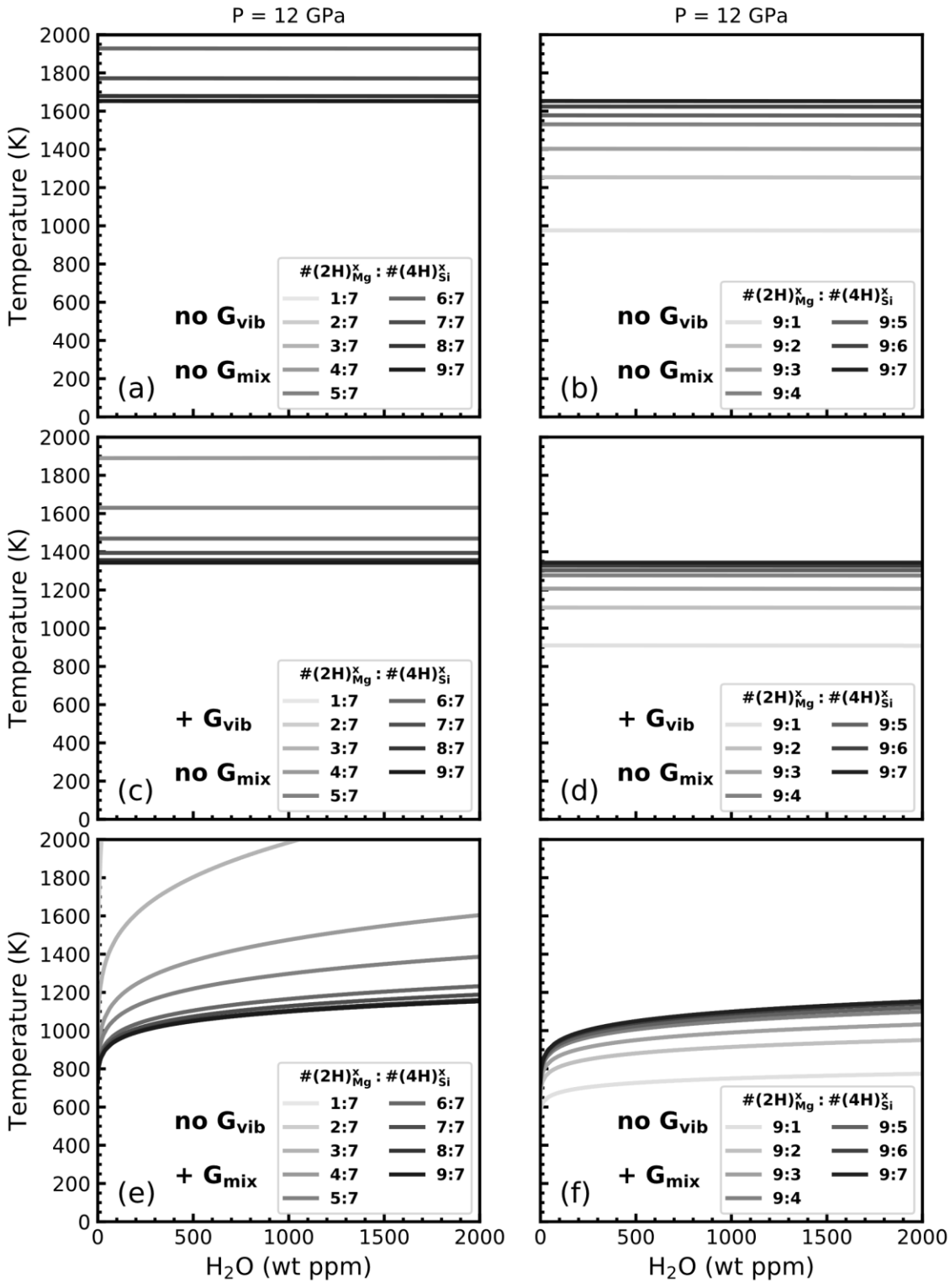

550